Highly-Dispersed Zinc Species on Zeolites for the Continuous and Selective Dehydrogenation of Ethane with CO_2 as a Soft Oxidant

Jiaxu Liu,* Ning He, Zhenmei Zhang, Jinpeng Yang, Xiao Jiang,* Zhuolei Zhang, Ji Su,* Miao Shu, Rui Si, Guang Xiong, Hong-bin Xie, and Gianvito Vilé*

ABSTRACT: We report herein the preparation, characterization, and catalytic performance of a series of heterogeneous catalysts featuring highly dispersed zinc sites on zeolitic SSZ-13 and ZSM-5 frameworks. The materials are evaluated in the CO_2-assisted oxidative ethane dehydrogenation, a very important reaction for the synthesis of platform chemicals. In particular, we find that $Zn_{2.92}$/SSZ-13 exhibits high reactivity in the conversion of C_2H_6 and CO_2 and high ethene selectivity. In line with the experimental results, we show that the selective character of the catalyst is due to the characteristic compositional structure of the support and its topology that can effectively confine CO_2 molecules. An in-depth molecular analysis via *operando* studies and DFT calculations shows that the rate-limiting step of the reaction with CO_2 is the second C−H bond dissociation to give C_2H_4. The addition of CO_2 effectively reduces the energy barrier of this step, favoring desorption of C_2H_4 while limiting byproduct formation. Overall, this work demonstrates the breakthrough potential of catalysts made of highly dispersed zinc species on zeolites in relevant transformations.

KEYWORDS: *reforming, oxidative dehydrogenation, ethane, ethylene, CO_2 conversion, zeolites, single-site catalysis*
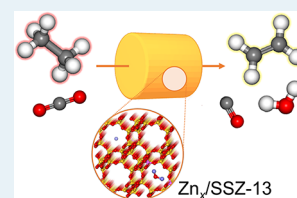
1. INTRODUCTION

As the economy and world population continue to rise, CO_2 emissions have reached 33.3 billion tons in 2019.[1] Thus, increasing endeavors are being paid to technologies that can capture, store, and/or utilize carbon dioxide, a gas that tends to accumulate in the atmosphere and is among the gases responsible for the "greenhouse effect".[2−9] Among those, methods that can catalytically convert CO_2 into value-added molecules are particularly interesting, since they can create an opportunity to convert waste into a commodity, while preventing it from entering the atmosphere.[10,11]

Catalytic hydrogenation of CO_2 to methanol,[12−14] formic acid,[15−17] and olefins[18−20] is often considered a promising approach for the direct utilization of this small molecule. However, the transportation, storage, and use of gaseous H_2 are associated with safety issues and logistical challenges.[21] Searching for alternative routes that utilize CO_2 in a cost-effective manner (such as hydrogen-free reaction routes) is crucial for realizing a catalytic waste to product platform.

Ethane dehydrogenation is an efficient and sustainable approach to convert ethane into ethylene, a primary platform molecule for the manufacture of polyethylene, ethylene glycol, and styrene among others.[22−30] C_2H_6 is the second largest component of shale gas and has a high content of hydrogen (75 mol %), which is only lower than that of methane (80 mol %) among alkanes. More importantly, the C−H bond of C_2H_6 is easier to break in comparison to that of CH_4, making it an alternative hydrogen source and a useful starting point for sustainable C−H activation in the absence of H_2.[28,30] However, the direct dehydrogenation of C_2H_6 is limited by

the thermodynamic equilibrium and is highly endothermic ($\Delta H°_{298} = +136.5$ kJ mol^{-1}), requiring extremely high temperatures (>900 °C) to happen. To overcome the excessive energy consumption of such a process, CO_2 has been recently proposed as a mild oxidant to alter the dehydrogenation pathway, on the basis of the reaction $C_2H_6 + CO_2 \rightarrow C_2H_4 + CO + H_2O$.[28,31−35] This would reduce the operating temperature to lower conditions (400−600 °C).[26,27] In addition, the presence of CO_2 as a reactant will also reduce the extent of coke (C) formation at high temperatures via the reverse Boudouard reaction ($CO_2 + C \rightarrow 2CO$), improving the stability of the catalysts.[28,29] Thus, the strategy to convert C_2H_6 in the presence of CO_2 is feasible and can supply valuable chemicals while mitigating detrimental CO_2 emissions.[36−38]

In the CO_2-assisted oxidative dehydrogenation of ethane (CO_2-ODHE), heterogeneous catalysts featuring metal-based particles of Ga, Fe, Ni, Pt, Co, and V deposited on a variety of supports, such as ZSM-5, SiO_2, TiO_2, Al_2O_3, SBA-15, MSU-x, clinoptilolite, MCM-41, and SAPO-34, have been reported.[22−38] Unfortunately, these catalysts show common unsatisfactory features, such as low CO_2 and C_2H_6 conversions and low C_2H_4 selectivity. For example, using CrO_x/NaZ50, it

is possible to obtain a C_2H_6 conversion of 65% and a CO_2 conversion of only 22% at 650 °C, leading to a C_2H_4 selectivity of ca. 50%.[39] Similarly, ball-milled hexagonal boron nitride prepared by oxidizing boron on the carbon nitride surface was found to catalyze the CO_2-ODHE with a high selectivity to C_2H_4 (92−96%) at 550 °C, but at very low C_2H_6 and CO_2 conversions (9%).[34] Obtaining a catalyst that is able to retain a high product selectivity with well-retained high C_2H_6 and CO_2 conversions is thus highly desirable.

In this work, we report the preparation, characterization, and catalytic performance of a series of SSZ-13 zeolitic catalysts containing isolated Zn species in the framework. SSZ-13, an aluminosilicate zeolite possessing CHA cages connected by an eight-membered ring with a small pore opening of 3.8 Å, was patented by Chevron in 1985.[40] In recent years, Cu-exchanged SSZ-13 has been applied for the selective catalytic reduction of NO_x.[41−44] One of the significant properties of SSZ-13 is its excellent hydrothermal stability, enabling the diesel exhaust temperature to rise well above 800 °C.[45] More importantly, Hudson et al.[46] found that SSZ-13 exhibits unconventional, highly selective CO_2 adsorption ability due to its unique pore structure. This indicates that its small pore can effectively confine CO_2 in the channel, which is expected to be beneficial for converting CO_2. On the basis of the above discussion, we propose that SSZ-13 is the ideal choice as a catalyst support for the CO_2-ODHE. The choice of depositing Zn on SSZ-13 is justified by the fact that Zn-modified zeolites have shown high efficiency for the dehydrogenation of short-chain hydrocarbons at relatively low temperatures.[47−49] The catalytic performance of Zn/SSZ-13 was compared with that of Zn-based catalysts featuring different zeolitic topologies, such as Zn/ZSM-5, Zn/MCM-22, and Zn/NaY. The experimental results further show the role of SSZ-13 in a superior CO_2-ODHE performance. The catalytic performance is then rationalized via density functional theory (DFT) calculations and *operando* experiments, unlocking the structure−performance relationships of these single-site zeolitic materials.

2. MATERIALS AND METHODS

2.1. Catalyst Preparation. NaSSZ-13 (herein indicated as NaS50) and NaZSM-5 (herein indicated as NaZ50) with a total SiO_2/Al_2O_3 ratio of 50 and a crystal size of approximately 1 μm were purchased from Dalian Ligong Qiwangda Chemical Technology. The NaMCM-22 and NaY zeolites were acquired from the Nankai Catalyst Co. Zinc nitrate $(Zn(NO_3)_2 \cdot 6H_2O,$ 99.9%) was purchased from Sinopac Chemical Reagent Co. Ltd. All chemicals were analytical grade and were used as such. Zn incorporation was attained by incipient wetness impregnation (IWI). The impregnation was performed at 80 °C for 60 min by using an aqueous zinc nitrate solution with variable Zn concentrations (1, 3, 5, and 9 wt %). The amount of aqueous solution to be used was chosen on the basis of the Zn loading to be expected in the materials and the pore volume of the zeolite. After impregnation, the samples were dried at 110 °C for 12 h and calcined at 650 °C for 6 h using air. Different calcination temperatures were explored (Figure S1), with no significant effects on the activity for a calcination temperature between 540 and 650 °C. Above this value, an activity drop was observed, likely due to catalyst restructuring at high temperatures.

2.2. Catalyst Characterization. X-ray diffraction (XRD) was recorded on a Rigaku D/max-2004 diffractometer with a Cu Kα source (40 kV, 100 mA), using a scanning speed of 2°

min^{-1} and in the 2θ range between 5 and 80°. X-ray fluorescence (XRF) was done on a Bruker SRS3400 analyzer equipped with a silicon drift detector. Nitrogen isotherms were measured at −196 °C on a Micromeritics ASAP 3020 instrument. The samples (380−830 μm sieve fraction) were evacuated at 340 °C for 5 h before analysis. The surface area was calculated using the Brunauer−Emmett−Teller (BET) method.[50] The pore volume was assessed at a p/p_0 value of 0.99, while micro- and mesoporosity were discriminated by the t-plot method.[51] Temperature-programmed desorption of ammonia (NH_3-TPD) was performed on a Quantachrome ChemBet 3000 chemisorb instrument. The solids (ca. 150 mg, 380−830 μm sieve fraction) were pretreated in He (99 wt % purity) at 600 °C for 1 h. Afterward, 5 vol % of NH_3/He (120 mL min^{-1}) was adsorbed at 100 °C for 30 min, followed by He purging (50 mL min^{-1}) at the same temperature for 30 min. The NH_3-TPD profiles were recorded in a 50 mL min^{-1} He flow by ramping the temperature from 100 to 600 °C at a rate of 16 °C min^{-1}. Temperature-programmed desorption of carbon dioxide (CO_2-TPD) was conducted on the same instrument. In particular, the solids (0.15 g) were pretreated in He at 450 °C for 1 h. CO_2-TPD was conducted by heating the samples from room temperature to 600 °C at a rate of 10 °C min^{-1} in 5 vol % CO_2/N_2 (120 mL min^{-1}). High-resolution transmission electron microscopy (HRTEM) was undertaken on an FEI (Tecnai F30 G2, The Netherlands) microscope. Fourier-transform infrared spectroscopy (FTIR) was conducted at room temperature wih a Nicolet 10 FTIR spectrometer (400−4000 cm^{-1}, 4 cm^{-1} optical resolution), equipped with a quartz IR cell and CaF_2 windows. A self-supporting thin wafer containing the zeolites (ca. 16 mg) was decontaminated for 4 h at 400 °C under vacuum (residual pressure 10^{-3} Pa). Afterward, the cell was cooled for sample measurement at room temperature. To examine the evolutions in the hydroxyl regions, the spectra were processed by subtracting from the measured sample spectra a background spectrum recorded in an empty IR cell in the absence of the catalyst. The spectra after NH_3 adsorption were obtained after 10 vol % NH_3/He (120 mL min^{-1}) adsorption at 150 and 300 °C for 30 min, followed by evacuation at 300 °C for 30 min. *Operando* Fourier transform infrared (FTIR) spectroscopy was employed to study the conversion of CO_2 and ethane (99 wt % purity) over pristine and Zn-modified NaS50 at 300 °C and atmospheric pressure. The catalysts were pressed into self-supporting thin wafers (1 cm^2), placed in the infrared cell, and activated at 400 °C for 4 h under vacuum (residual pressure 10^{-3} Pa). The spectra were recorded in the 4000−1000 cm^{-1} region, using a resolution of 4 cm^{-1} and 64 scans. The effluent from the IR cell was analyzed by a quadrupole mass spectrometer (Omnistar, 1−200 amu, QMS 200). X-ray absorption fine structure (XAFS) spectroscopy at the Zn K (E_0 = 9659 eV) edge was carried out at the BL14W1 beamline of he Shanghai Synchrotron Radiation Facility (SSRF). The data were recorded in the fluorescence mode with a Lytle ion chamber. The energy was calibrated on the basis of the absorption edge of Zn foil. For X-ray absorption near edge structure (XANES), the experimental absorption coefficients as a function of energies $\mu(E)$ were processed by background subtraction and normalization measures, with E_0 = 9659 eV for all of the studied samples. For extended X-ray absorption fine structure (EXAFS), the Fourier transform (FT) data in the R space was examined by applying a first-shell approximate model for Zn−O, Zn−Zn, and Zn−Al. The passive electron

Table 1. Properties of Zn-Modified NaS50 Catalysts

catalyst	code	$SiO_2/Al_2O_{3_{bulk}}$[a]	S_{BET}[b] ($m^2\ g^{-1}$)	S_{micro}[c] ($m^2\ g^{-1}$)	V_{pore} ($cm^3\ g^{-1}$)	V_{micro} ($cm^3\ g^{-1}$)	Brønsted acid sites[d] ($mmol\ g^{-1}$)	Lewis acid sites[d] ($mmol\ g^{-1}$)
NaSSZ-13	NaS50	50	698	666	0.34	0.30	0.01	0.009
$Zn_{0.83}$/NaSSZ-13	$Zn_{0.83}$/NaS50	50	688	654	0.34	0.30	0.01	0.010
$Zn_{1.70}$/NaSSZ-13	$Zn_{1.70}$/NaS50	50	674	638	0.33	0.29	0.02	0.012
$Zn_{2.92}$/NaSSZ-13	$Zn_{2.92}$/NaS50	50	656	617	0.33	0.28	0.02	0.011

[a]XRF. [b]BET method applied to the N_2 isotherm. [c]t-plot method applied to the N_2 isotherm. [d]Determined by NH_3-FTIR.
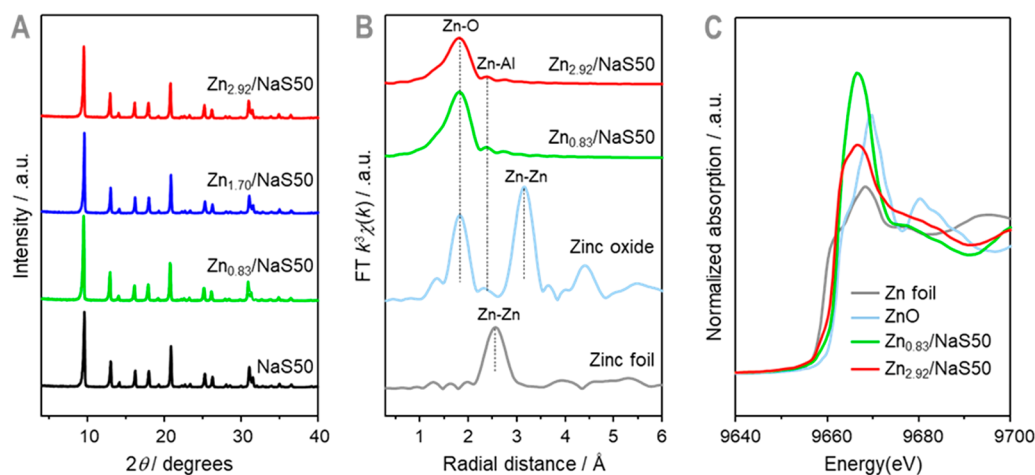

Figure 1. (A) X-ray diffraction patterns of the different catalysts. EXAFS Zn K-edge radial distribution functions (B) and Zn K-edge extended X-ray absorption near-edge spectra (C) of Zn foil, ZnO, NaS50, and Zn_x/NaS50 catalysts with variable Zn loadings.

factors, S_0^2, resulted by fitting the experimental data on Ni foils and fixing the coordination number of Zn−Zn to be 6 + 6. The parameters describing the electronic properties (e.g., correction to the photoelectron energy origin, E_0) and local structure environment, including the coordination number, bond distance (R), and Debye−Waller factor around the absorbing atoms, were left to vary during the fit process. The fitted ranges for k and R spaces were selected to be k = 3−12 Å^{-1} with R = 1.1−4.0 Å (k^3 weighted).

2.3. Catalyst Performance. A fixed-bed continuous-flow setup was employed to study the CO_2-ODHE performance of pristine and Zn-modified catalysts. In particular, the catalyst (2.0 g, 20−40 mesh particles) was loaded in a stainless-steel microreactor (600 mm length, 10 mm internal diameter), equipped with a thermocouple to monitor the catalyst bed temperature. The remaining part was filled with silica particles with a diameter of 10−20 mesh. Prior to the reaction, the catalyst was kept at 540 °C for 1 h in N_2 flow (1 mL min^{-1}) to remove any adsorbed water. The feedstock was composed of 5% ethane, 5% CO_2, and 90% helium (C_2H_6:CO_2:He = 1:1:18, with no O_2 present in the feed), and the flow was controlled by mass-flow controller. The hydrocarbon products were analyzed with a flame ionization detector (FID), while the presence of hydrogen and carbon monoxide was assessed by using a thermal conductivity detector (TCD).

2.4. Computational Method. As is shown in Figure S2, the calculated model with 48T obtained by cutting the periodic CHA-type zeolite was employed for the calculations. In particular, the dangling bonds were saturated with H atoms pointing to the next lattice oxygen atom, and the Si−H bond was set to a length of 1.46 Å. The calculations were performed with the Gaussian 09 program package.[52] To improve the energy properties and consider the effect of the entire zeolite framework on the reaction mechanism, a two-layer scheme ONIOM model was employed.[53] The surface and catalytically active region were treated with the long-range corrected hybrid ωB97XD density functional developed by Chai and Head-Gordon, along with the 6-31+G(d,p) basis set for accuracy.[54] In fact, ωB97XD has been found to be more reliable for the calculation of the dispersion as well as charge transfer (CT) excited states in comparison to earlier density functionals. The universal force field (UFF) was employed to study the regions away from the active center. For all DFT calculations, the positions of the terminal SiH_3 atoms were fixed, while the remaining atoms were left to relax. Many experimental and theoretical studies have indicated that the distribution of Al in the framework of a zeolite would influence the species of metal ions located on the catalysts. On the basis of previous experimental data,[55] there are two possible Zn species: zinc ion Zn^{2+} and oxidic zinc ion $[Zn-O-Zn]^{2+}$. Therefore, all possible models with different locations of Al and Zn species were considered. As shown in Tables S1 and S2 in the Supporting Information, Models 6M_1 and 8M_1 with Zn^{2+} and $[Zn-O-Zn]^{2+}$, respectively, are the two most preferable models from the view of thermodynamics. Thus, in this work, these two models were selected to investigate the reaction mechanism. The transition state structures were characterized by frequency calculations with one imaginary frequency. When necessary, the intrinsic reaction coordinate method was applied to find the two minima connected by a transition state. The single-point energy calculations in the optimized model were further refined at the theoretical level of ωB97XD/6-311++G(d, p).

3. RESULTS AND DISCUSSION

3.1. Characterization of the Zn-based NaS50 Catalysts. A variety of Zn/NaSSZ-13 catalysts (herein indicated as Zn/NaS50) have been prepared in this study. Table 1 includes a list and the codes assigned to each sample. Figure 1A depicts the XRD patterns of the pure and Zn-modified NaS50 samples. The parent zeolites display sharp characteristic peaks assigned to the corresponding CHA topological framework. The reflections remain evidenced upon the introduction of the Zn phase. This indicates a high Zn dispersion and the absence of any structural alteration upon metal incorporation. Such a result has been confirmed by HRTEM micrographs (Figure 2),
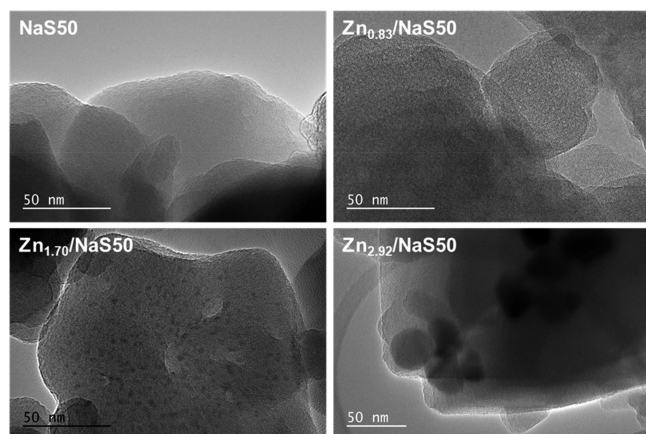

Figure 2. Transmission electron micrographs of NaS50 and different Zn-based NaS50 catalysts. The micrographs depict the presence of isolated Zn atoms at low Zn concentration, and ZnO nanoparticles at high Zn concentration. Two different surface models have been used to discriminate chemical reactivities over the different nanocatalysts (vide infra).

which show highly dispersed zinc species and no zinc oxide particles for the $Zn_{0.83}$/NaS50 catalyst. When the loading is increased above 1 mol %, small ZnO nanoclusters are formed. The particles, however, are too small to give sharp XRD reflections in Figure 1A. To verify the electronic and local coordination structures of the zinc species on SSZ-13, the XAFS technique was used for the $Zn_{0.83}$/NaS50 and $Zn_{2.92}$/NaS50 catalysts. EXAFS (Figure 1B) gives further insights into

the direct structural information on the local coordination of Zn in the zeolites. Over the Zn foil, a peak at 2.6 Å is observed, corresponding to Zn−Zn nearest neighbors in the Zn metal. In contras, two peaks at 1.95 and 3.1 Å are evidenced over ZnO, which respectively resemble the Zn−O distance of a tetrahedral ZnO_4 arrangement and the second shell of Zn−Zn from Zn−O−Zn that is characteristic of the hexagonal bulk zinc oxide. For Zn-modified NaSSZ-13 zeolites, the absence of peaks at 3.1 Å suggests that the main portion of zinc in these samples is present in the form of Zn^{2+} cations in an "oxidized" phase. Therefore, isolated Zn species without any coordinated Zn−Zn sites characterize the Zn/zeolite catalysts. The XANES data for the Zn K edge in Figure 1C corroborates the prevailing presence of Zn(II) in these samples, resulting in similar edge jumps from 9650 to 9665 eV. The XANES profiles in the range of 9660−9700 eV exhibit similar shapes between $Zn_{0.83}$/NaS50 and $Zn_{2.92}$/NaS50 catalysts, indicating analogous coordinated structures between these samples.

According to the nitrogen physisorption data in Table 1, the microporous surface area and microporous volume of the modified samples gradually decrease as the amount of Zn increases. It is deduced that most of the Zn species over Zn/NaS50 are located inside the channel of the zeolite, thus affecting the surface area and the (micro)pore volume of the materials. In particular, the absence of any pore volume variation between NaS50 and $Zn_{0.83}$/NaS50 and the 10% drop of the same values for $Zn_{1.70}$/NaS50 and $Zn_{2.92}$/NaS50 signify a reduction in the pore volume, which is likely in the form of partial pore occlusion due to the presence of tiny ZnO nanoclusters (Figure 2).

The CO_2 adsorption isotherms measured at 298 K are shown in Figure 3A. The NaS50-based samples, without and with Zn, exhibit a significant CO_2 adsorption capacity, which indicates that the SSZ-13 framework can accommodate large quantities of CO_2 in spite of the zeolite small pore opening (0.38 Å, to be compared to a CO_2 van der Waals diameter of 0.2 Å[56]). Similarly, from the CO_2-TPD results (Figure 3B), it appears that all Zn/NaS50 samples have an intense desorption peak around 100−150 °C. No variation in CO_2-TPD adsorption abilities is detected on the basis of the variable textural properties of the materials. Figure 4A depicts NH_3-TPD profiles with the information on the acidic strength of the zeolites. The NaS50-based catalysts have weak acid sites, as
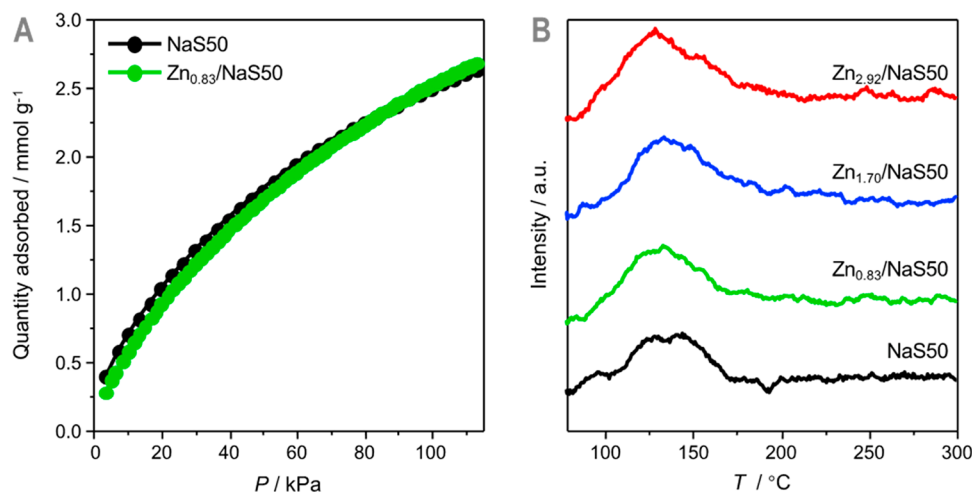

Figure 3. CO_2 physisorption (A) and CO_2 temperature-programmed desorption (B) of different Zn-based NaS50 catalysts.
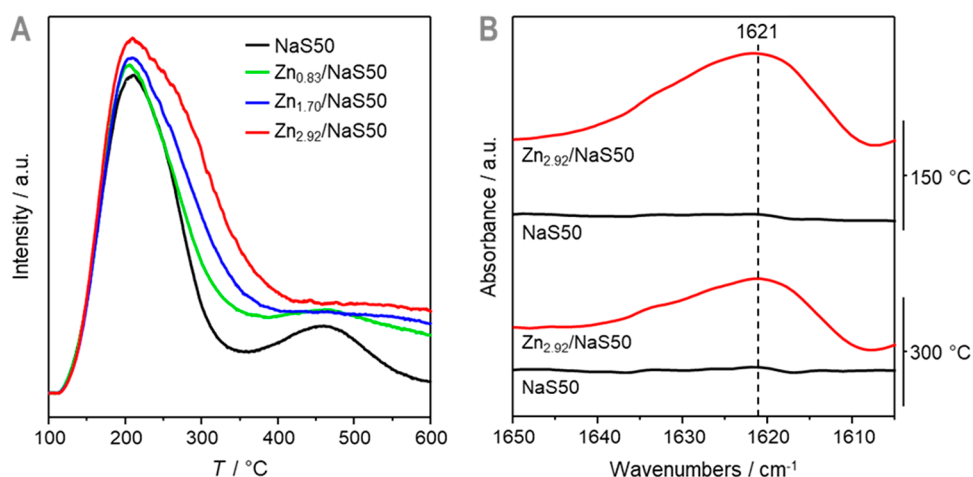
Figure 4. (A) NH_3 temperature-programmed desorption of different Zn-based NaS50 catalysts. (B) Fourier-transform infrared spectra of NaS50 and $Zn_{2.92}$/NaS50 catalysts prior to and after NH_3 adsorption at different temperatures. The FTIR peak at 1621 cm^{-1} points to the presence of Lewis acid sites as a result of the incorporation of Zn into the zeolite framework.
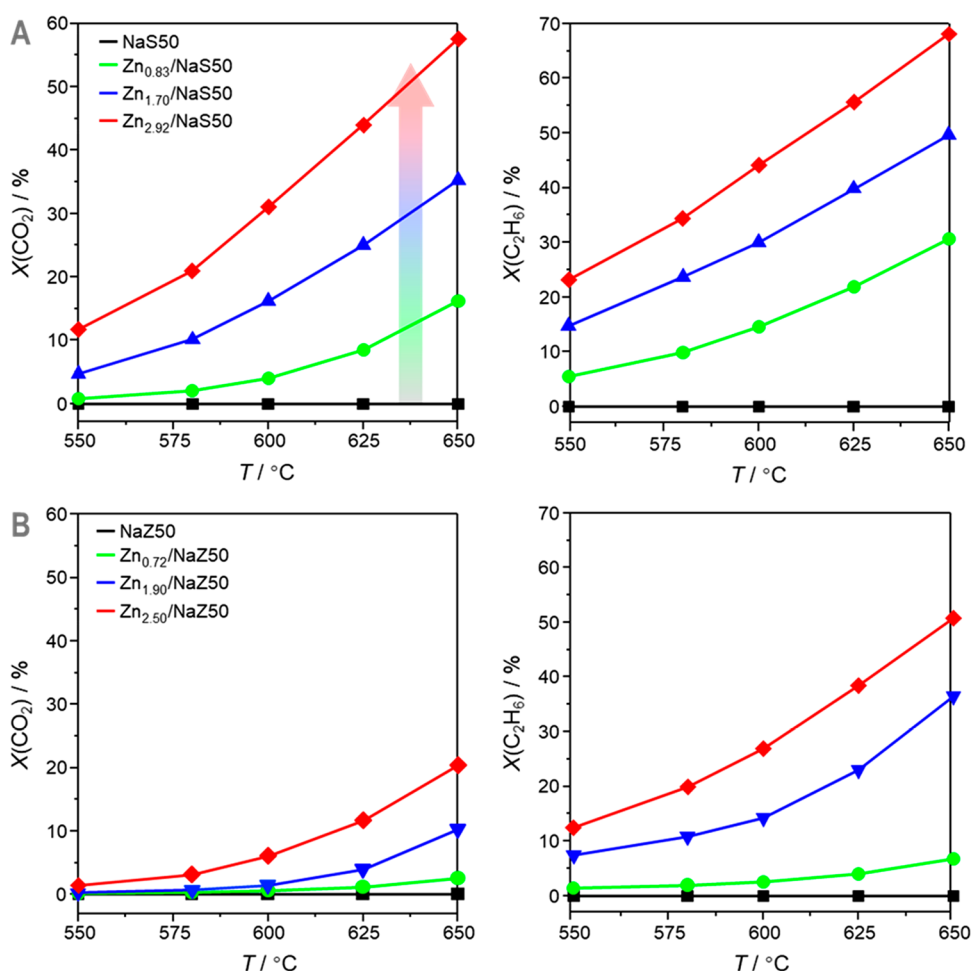

Figure 5. Influence of the Zn loadings on the conversion of CO_2 and C_2H_6 over different Zn-based NaS50 (A) and NaZ50 (B) zeolites. Conditions: temperature 550−650 °C, pressure 0.1 MPa, CO_2:C_2H_6 = 1, and GHSV = 3600 mL h^{-1} g$_{cat}$$^{-1}$.

confirmed by the low-temperature desorption peak around 100−300 °C. A relatively small fraction of strong acid sites is present on the CHA framework at high concentrations of Zn in the sample. To differentiate Lewis and Brønsted acid sites, NH_3 adsorption and FTIR spectroscopy were performed, as shown in Figure 4B. The adsorbed species at 1621 cm^{-1} over

the Zn-containing NaS50 samples is assigned to NH_3 molecules on Lewis acid sites.[28] Since these sites are absent on the pristine materials, these acid sites likely originate from the incorporation of zinc species into the NaS50 structure. A quantification of the acid sites is reported in Table 1, further
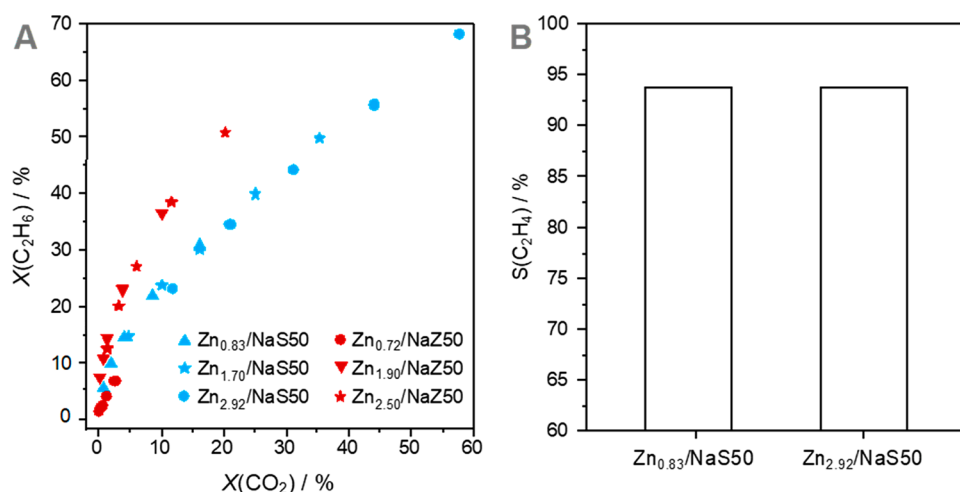
Figure 6. (A) Conversion of C_2H_6 as a function of the conversion of CO_2 over different Zn-based NaS50 and NaZ50 zeolites. Conditions in (A): temperature 550−650 °C, pressure 0.1 MPa, CO_2:C_2H_6 = 1, and GHSV = 3600 mL h^{-1} g$_{cat}$$^{-1}$. (B) Selectivity to C_2H_4 over different Zn-based NaS50 catalysts, at a CO_2 conversion level of 10%. Conditions in (B): temperature 650 °C, pressure 0.1 MPa, CO_2:C_2H_6 = 1, and GHSV = 3600−7200 mL h^{-1} g$_{cat}$$^{-1}$.

corroborating an increased presence of strong Lewis acid sites over the high-loading Zn samples.

3.2. Evaluation of the Zn-Based NaS50 Catalysts in CO_2-ODHE. The NaS50 catalysts with different loadings of Zn have been investigated in CO_2-assisted oxidative C_2H_6 dehydrogenation (Figure 5A). In comparison with the parent zeolite without any incorporation of Zn species, which is inactive in the reaction (see also Figure S3), the addition of Zn significantly increases the C_2H_6 and CO_2 conversions. The conversion of both reactants can be linearly correlated with the Zn loading, indicating that Zn plays a catalytic role in this reaction. The absence of any activity in the parent zeolite is a very distinctive characteristic to discriminate between a doped and a single-site catalyst. In our case, since the bare zeolitic framework is inactive, we can confidently state that the Zn- and ZnO-based materials function as "single-site catalysts".[26,57,58] It is, in fact, the presence of highly dispersed metal (oxide) sites that contributes to the observed activity. When this happens, alloys, oxides, and isolated metal species function as single-site catalysts.[58] Specifically, Zn$_{2.92}$/NaS50 stands out as the most active catalyst. In fact, at 650 °C, the CO_2 and C_2H_6 conversions over Zn$_{2.92}$/NaS50 are ca. 60% and 70%, respectively. Figure S4 shows the Arrhenius plot for this material and the experimentally determined activated energy from the linear regression. The obtained value (45 kJ mol^{-1}) is inferior to the values reported in the literature (Table S3),[28,29] pointing to a more favorable energy barrier over Zn-doped NaS50 samples. Figure 6A shows the correlation between the conversion of C_2H_4 and that of CO_2 for the different Zn/NaS50 samples. In the case of Zn$_{2.92}$/NaS50, the ratio between the conversion of CO_2 and that of C_2H_6 is around 0.86, which is close to the ideal value (i.e., 1), representing an equivalent coconversion of CO_2 and C_2H_6. In such a situation, we expect the catalyst to be highly selective, since both reactants interact on the basis of the reaction stoichiometry $C_2H_6 + CO_2 \rightarrow C_2H_4 + CO + H_2O$.[22−35] As reported, the activation of CO_2 needs the presence of surface hydrogen or ZnOH.[26] These reactive intermediates are formed after C_2H_6 activation,[26−30] explaining the reason why the conversion of CO_2 is slightly lower than that of C_2H_6. To discuss the product selectivities, it is critical to compare catalysts under isoconversional

conditions.[59] This has been done, and Figure 6B presents the selectivity−conversion plot, where two different Zn/NaS50 catalysts are compared under kinetic conditions: namely, at a CO_2 conversion of ca. 10%. The figure nicely shows the exceptional behavior of the Zn/NaS50 catalysts, with an outstanding C_2H_4 selectivity well above 90%. The complete C_2H_4 selectivity patterns observed over the different Zn-containing NaS50 catalysts at various temperatures and higher degree of conversion are depicted instead in Figure S5 in the Supporting Information. It is important to recognize that the high selectivity is dependent not only on the catalyst properties (as in this case) but also on the selection of a CO_2:C_2H_6 ratio of 1. In the latter case, when a lower ratio is selected, some side reactions are inevitable, including hydrogenolysis and/or steam reforming of C_2H_6 to generate CH_4, as reported elsewhere.[60,61]

The catalytic performance of Zn/NaS50 was evaluated as a function of time on stream (TOS) (Figure S6). The illustration, in particular, depicts the conversion and selectivity obtained over Zn$_{0.83}$/NaS50 and Zn$_{2.92}$/NaS50. The two catalysts were chosen to evaluate TOS behaviors over 200 min of reaction, at low and high metal loadings. As shown in Figure S6, Zn$_{0.83}$/NaS50 exhibits a stable catalytic performance, as the C_2H_6 conversion and C_2H_4 selectivity remain constant at ca. 30% and around 95−98%, respectively. This points to the great stability of isolated Zn^{2+} species. Instead, for Zn$_{2.92}$/NaS50, the activity slightly decreases as the TOS increases, implying a partial deactivation of ZnO nanoclusters. We can deduce that lower Zn loadings lead to the atomic incorporation of Zn on the zeolite framework, thus giving a stable catalytic behavior.

The importance of CO_2 in the reaction and its role in shifting the oxidative dehydrogenation of C_2H_6 to more selective paths have been rationalized by conducting the same reaction in the absence of CO_2 and that using O_2 as an oxidant. For comparison, Zn$_{2.92}$/NaS50 was selected as the catalyst, and the partial pressure of the oxidants (i.e., CO_2 and O_2) remained unchanged. As shown in Table S4, O_2 is a stronger oxidant, providing a higher fraction of CO_x byproducts. Again, this corroborates the importance of CO_2 as a mild oxidant in achieving better dehydrogenation performance.

Finally, in zeolites, the catalytic performance is strongly dependent on the topological structure of the material.[38,39]
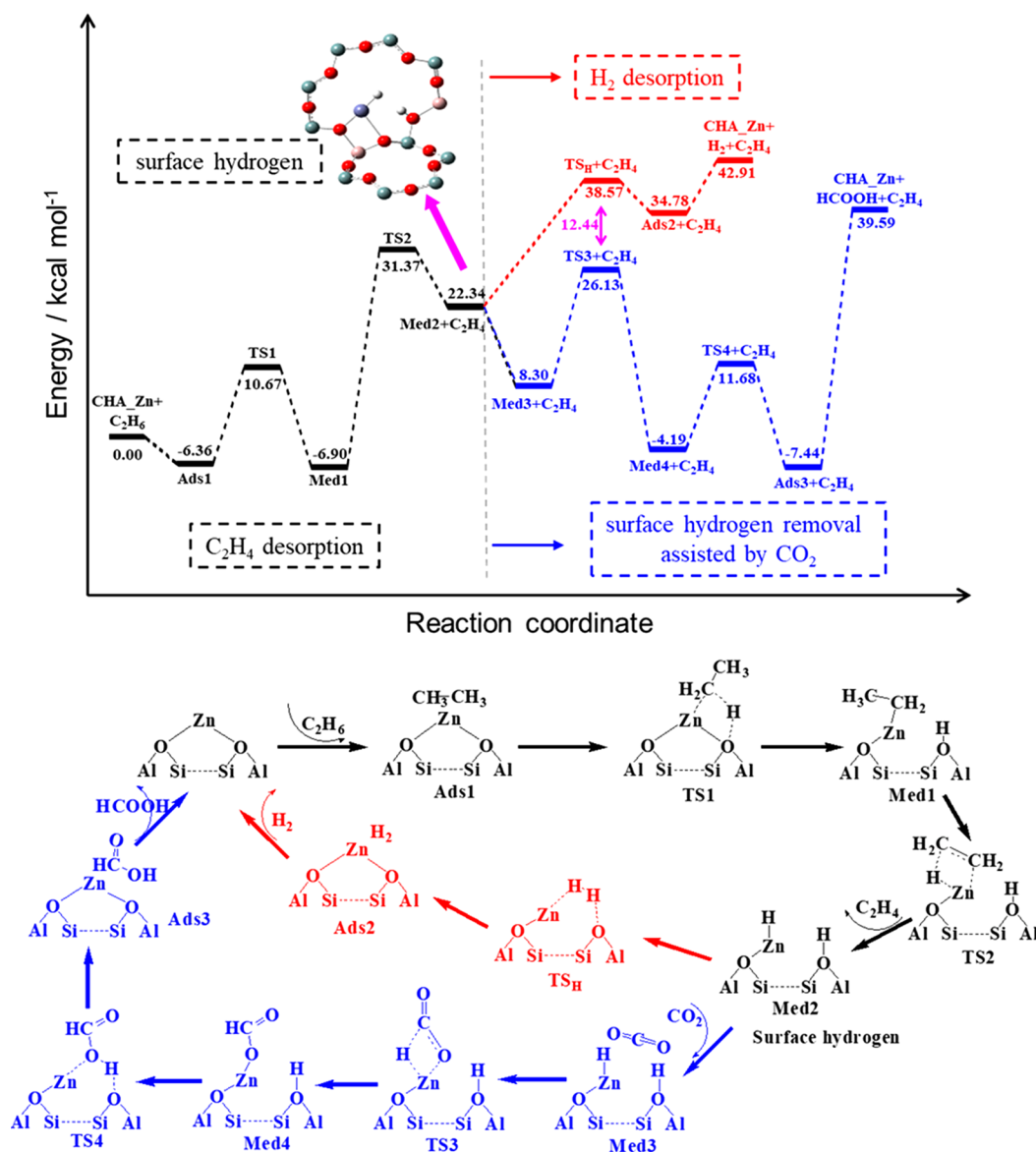
Figure 7. Energy profiles for the conversion of ethane on Zn^{2+}, without and with CO_2 as a soft oxidant. The color code in the energy profile refers to the mechanism and the elementary steps illustrated below.

Hence, a series of Zn-containing zeolite catalysts have been prepared and their activities evaluated in the CO_2-ODHE, also in an effort to compare with the performance of $Zn_{2.90}/NaS50$. The characterization results of these materials are reported in Table S5 and Figure S7, while the complete activity data are given in Figures S8 and S9. In particular, the Zn-doped NaS50 catalyst evidently outperforms the others in Zn-loading-based activity, which decreases in the sequence NaS50 > NaZ50 ∼ NaMCM-22 > NaY (Figure S8). This is opposite to that of the zeolite pore diameter (SSZ-13 (0.38 Å) < ZSM-5 and MCM-22 (0.55 Å) < Y (0.78 Å)), pointing to the fact that zeolites with small pore openings are preferable due to a more controlled adsorption of CO_2. A closer understanding at the importance of the zeolite pore diameter can be grasped by comparing the activity of the NaS50-based samples in Figure 5A with the NaZ50-based catalysts in Figure 5B. Even if the activity increases with the increased Zn loading, the NaS50-based catalysts stand out as the most active samples. In fact, at 650 °C, the CO_2 and C_2H_6 conversions over $Zn_{2.92}/NaS50$ are ca. 20−30% higher than that over the NaZ50 counterparts. In

addition to being less active, the NaZ50 samples are also less selective. As shown in Figure 6A, the ratio between the degrees of conversion of ethane and CO_2 is much below the ideal value (i.e., 1), representing an equivalent coconversion of CO_2 and ethane. In such a situation, we expect the catalyst to be less selective, generating methane. This is confirmed by the selectivity data in Figure S9 and proves the importance of selecting the correct zeolite framework.

3.3. Molecular-Level Understanding of the Catalytic Effects *via* DFT and *Operando* Studies. To obtain an in-depth understanding of the catalytic data and rationalize the role of CO_2 in the dehydrogenation of C_2H_6, advanced spectroscopic characterizations and DFT calculations have been performed to evaluate, with and without CO_2, the energy surfaces of the Zn-based single-site catalysts. On the basis of EXAFS data (Figure 1), two calculated models, $[Zn−O−Zn]^{2+}$ and Zn^{2+}, which respectively represent zinc oxide and zinc ion located on SSZ-13 zeolites, have been used to investigate the reaction. In particular, $[Zn−O−Zn]^{2+}$ represents the active sites on the nanoclusters of $Zn_{1.70}/NaS50$ and $Zn_{2.92}/NaS50$,
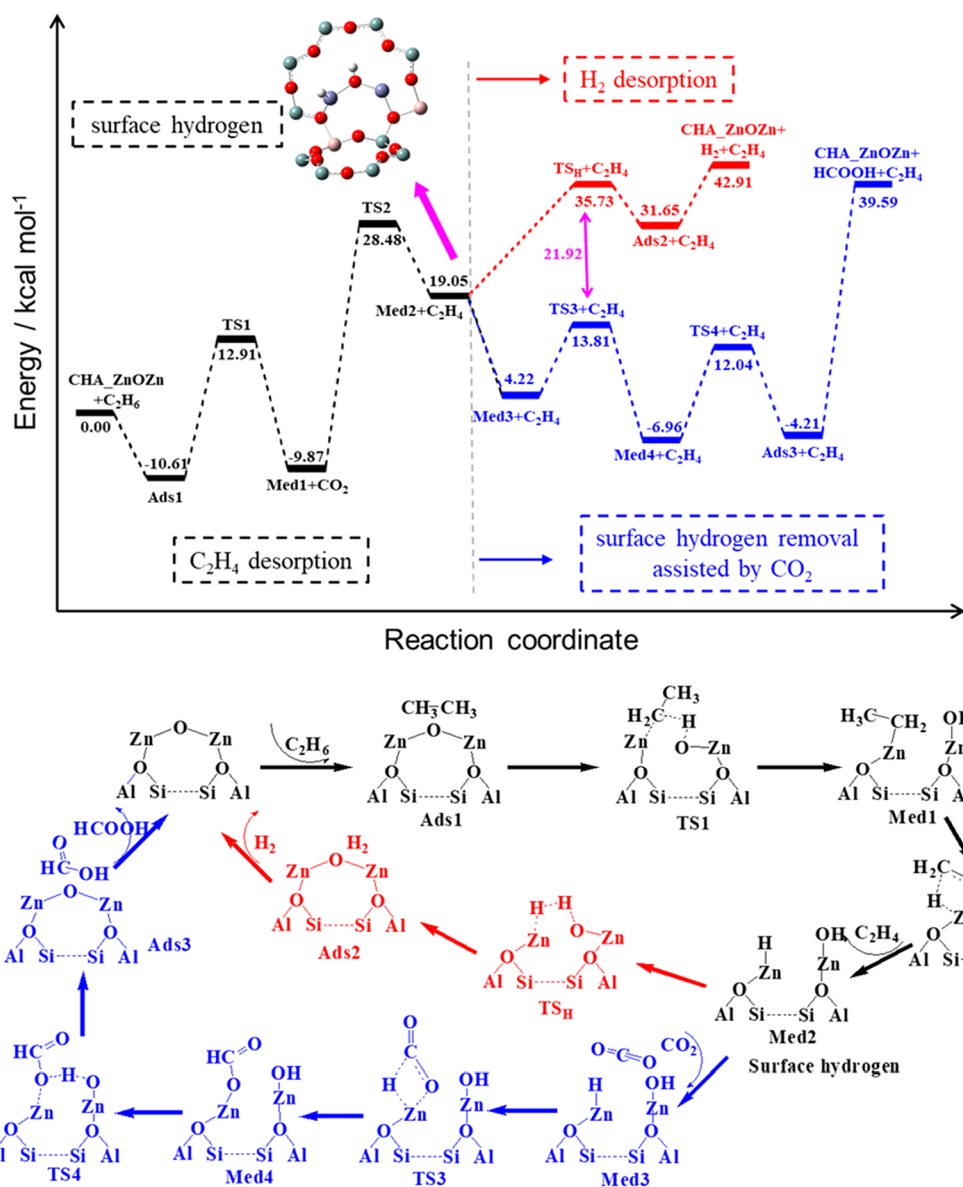
Figure 8. Energy profiles for the conversion of ethane on $[Zn-O-Zn]^{2+}$, without and with CO_2 as a soft oxidant. The color code in the energy profile refers to the mechanism and the elementary steps illustrated below.

while Zn^{2+} represents the active sites on the atomically isolated Zn species of $Zn_{0.83}/NaS50$.

DFT shows that the dehydrogenation mechanism of C_2H_6 contains two parts: (i) C_2H_6 activation to desorb C_2H_4 and (ii) surface hydrogen removal. Specifically, after the physical adsorption, C_2H_6 is initially dissociated on the active sites through C−H bond cleavage, leading to the formation of the ethyl intermediate and a transient Brønsted acid zinc hydroxyl group (ZnOH). Then, the ethyl intermediate goes through the second C−H bond cleavage to form the adsorbed C_2H_4* and release C_2H_4, leaving Zn−H on the surface of the catalyst. Subsequently, the desorption of H_2 occurs.

Figures 7 and 8 present the compared energy profiles for the two models. The desorption of H_2 is the most energy demanding step on both surfaces, requiring about 38.57 and 35.73 kcal mol^{-1} on Zn^{2+} and $[Zn-O-Zn]^{2+}$, respectively. Interestingly, the existence of CO_2 effectively reduces the energy barriers required for the surface hydrogen removal. In fact, the addition of CO_2 on the $[Zn-H^-]^+$ moiety generates

$[Zn-COOH]^+$, which only needs to overcome a barrier of 26.13 kcal mol^{-1} for Zn^{2+} and that of 13.81 kcal mol^{-1} for $[Zn-O-Zn]^{2+}$. The scheme of the overall reaction mechanism for the CO_2-ODHE is depicted as well. The major difference from a standard C_2H_6 dehydrogenation without CO_2 lies in the second C−H bond dissociation to desorb C_2H_4, which is the rate-limiting step for the CO_2-ODHE route. The addition of CO_2 effectively reduces the activation barrier of the surface hydrogen removal, which is favorable to the removal of surface hydrogen to avoid hydrogenolysis to undesired CH_4. It is worth noting that the energy barrier of surface hydrogen removal for $[Zn-O-Zn]^{2+}$ is decreased more (i.e., ca. 21.92 kcal mol^{-1}) than that of Zn^{2+} (i.e., ca. 12.44 kcal mol^{-1}).

To verify the reliability of calculated reaction mechanism and provide a clear picture of the dynamic surface processes involved in gas/solid heterogeneous catalysis under real reaction conditions, *operando* dual-beam Fourier transform infrared spectrometry (DB-FTIR) was performed under the conditions of C_2H_6 with and without CO_2 over $Zn_{2.92}/NaS50$
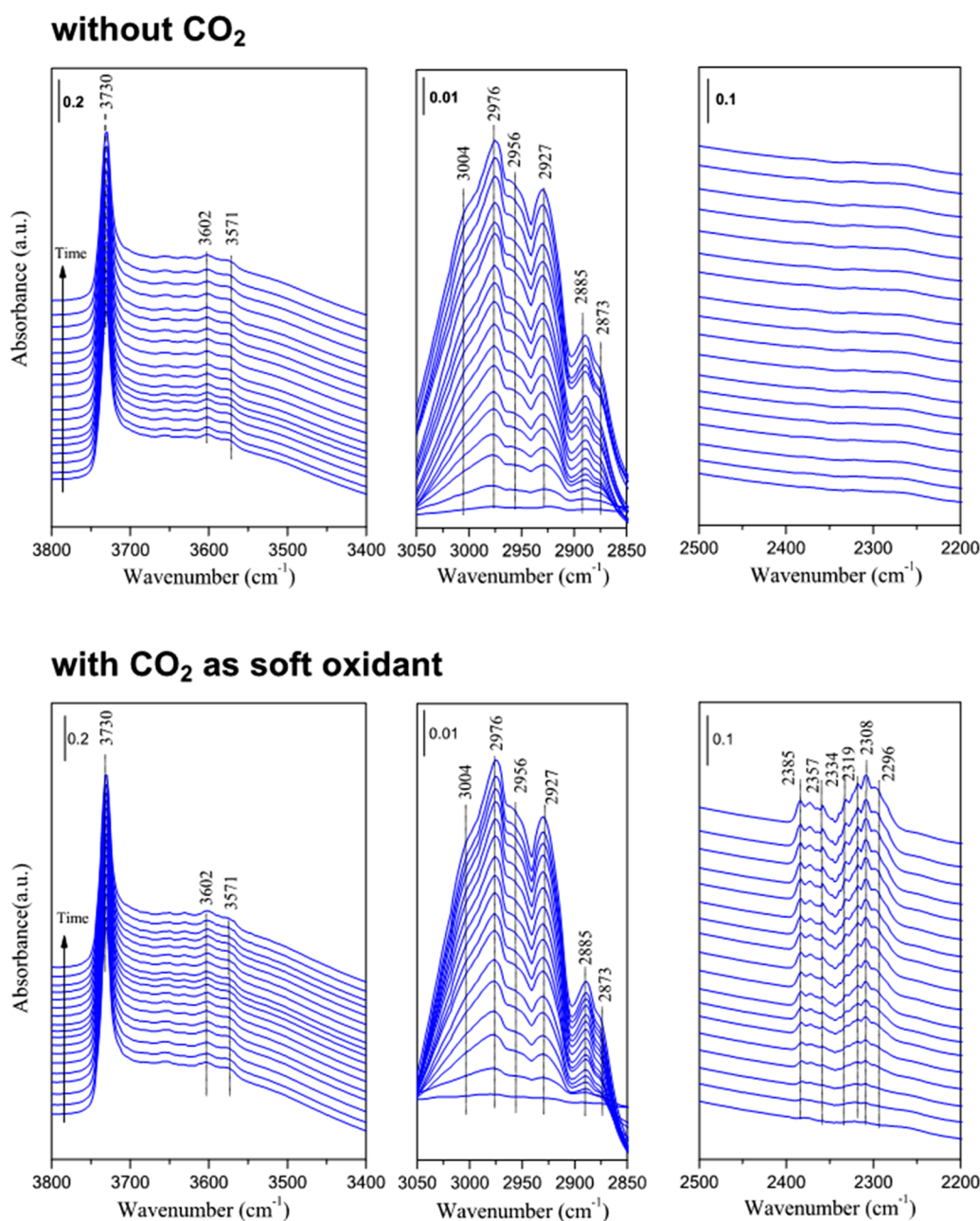
Figure 9. Selected spectra of ethane conversion over $Zn_{2.92}/NaS50$ at 300 °C, 0.1 MPa, and GHSV = 3600 mL h^{-1} g_{cat}^{-1} obtained using a DB-FTIR instrument in a flowing mixture of ethane and helium gas (2% ethane in helium) for 50 min, without and with CO_2 as a soft oxidant ($CO_2:C_2H_6 = 1$).

at 300 °C. As shown in Figure 9, the IR peaks at 3730, 3602, and 3571 cm^{-1}, which can be ascribed to O−H stretching vibrations, and the peaks at 2800−3000 cm^{-1}, which are attributed to the C−H stretching vibrations, are similar for the two reaction conditions. This indicates that the mechanisms of catalytic oxidative dehydrogenation of ethane are similar, independent of the presence of CO_2. However, a characteristic stretching vibration in the region 2385−2296 cm^{-1}, typically assigned to $HCOO^-$, is only observed on cofeeding CO_2 in the reaction mixture, and methane acid as an intermediate product was also detected in the effluent of DB-FTIR by mass spectroscopy (Figure 10). This observation is aligned with the DFT calculations, in which formic acid is proposed as an intermediate formed during the regeneration of surface active sites: namely, Zn^{2+} and $[Zn−O−Zn]^{2+}$.

4. CONCLUSION

This study has investigated the CO_2-mediated oxidative dehydrogenation of C_2H_6 over a family of heterogeneous catalysts made of highly dispersed Zn species entrapped in a zeolite carrier. Among the catalysts with various Zn loadings, $Zn_{2.92}/NaS50$ exhibits excellent catalytic performance for the conversion of C_2H_6, particularly with a uniquely high CO_2/C_2H_6 conversion ratio close to the ideal case of 1. In comparison to Zn-based catalysts made using other zeolites, $Zn/NaS50$ stands out as an active and selective material, owing to its unique channel structure that can effectively confine CO_2, increasing the activity and suppressing any side reaction. The Zn-containing NaS50 catalysts also exhibit good hydrothermal stability. DFT calculations demonstrate that such
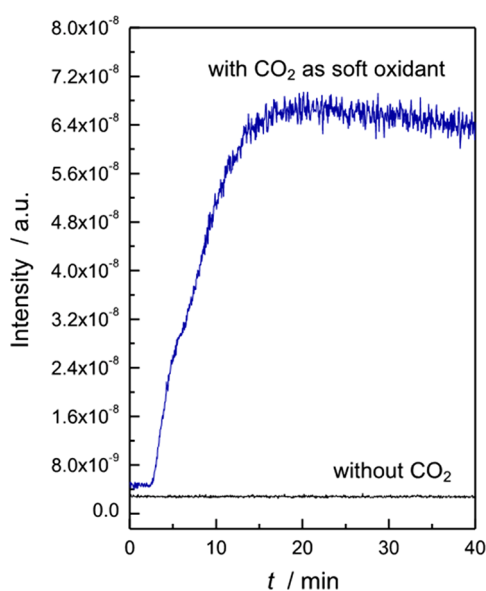
Figure 10. Mass spectra from the DB-FTIR effluent without (black line) and with (blue line) CO_2 as a soft oxidant. Conditions are as in Figure 9.

outstanding behavior can be correlated with the rate-limiting step for the dehydrogenation of C_2H_6 with CO_2, which is the second C–H bond dissociation to desorb C_2H_4. The addition of CO_2 effectively reduces the energy barrier of the surface hydrogen removal, avoiding hydrogenolysis to produce CH_4. Overall, this work not only reports single-site catalysts based on zeolites but also demonstrates a promising approach to efficiently convert both CO_2 and C_2H_6 by using Zn-containing NaS50 as an effective catalyst.

ASSOCIATED CONTENT

Supporting Information

The Supporting Information is available free of charge at https://pubs.acs.org/doi/10.1021/acscatal.1c00126.

Additional characterization data of the materials (PDF)

AUTHOR INFORMATION

Corresponding Authors

Jiaxu Liu − *Department of Catalytic Chemistry and Engineering, State Key Laboratory of Fine Chemicals, Dalian University of Technology, 116024 Dalian, People's Republic of China;* orcid.org/0000-0003-0815-3979; Email: liujiaxu@dlut.edu.cn

Xiao Jiang − *Chemical Sciences Division, Oak Ridge National Laboratory, 37831 Oak Ridge, Tennessee, United States;* orcid.org/0000-0002-4902-1828; Email: jiangx@ornl.gov

Ji Su − *Materials Sciences Division, Molecular Foundry, Lawrence Berkeley National Laboratory, 94720 Berkeley, California, United States;* Email: jisu@lbl.gov

Gianvito Vilé − *Department of Chemistry, Materials, and Chemical Engineering "Giulio Natta", Politecnico di Milano, 20133 Milano, Italy;* orcid.org/0000-0003-0641-8590; Email: gianvito.vile@polimi.it

Authors

Ning He − *Department of Catalytic Chemistry and Engineering, State Key Laboratory of Fine Chemicals, Dalian*

University of Technology, 116024 Dalian, People's Republic of China

Zhenmei Zhang − *Department of Catalytic Chemistry and Engineering, State Key Laboratory of Fine Chemicals, Dalian University of Technology, 116024 Dalian, People's Republic of China*

Jinpeng Yang − *Department of Catalytic Chemistry and Engineering, State Key Laboratory of Fine Chemicals and Key Laboratory of Industrial Ecology and Environmental Engineering, Department of Environmental Science and Technology, Dalian University of Technology, 116024 Dalian, People's Republic of China*

Zhuolei Zhang − *Materials Sciences Division, Molecular Foundry, Lawrence Berkeley National Laboratory, 94720 Berkeley, California, United States*

Miao Shu − *Shanghai Synchrotron Radiation Facility, Shanghai Institute of Applied Physics, Chinese Academy of Sciences, 201204 Shanghai, People's Republic of China*

Rui Si − *Shanghai Synchrotron Radiation Facility, Shanghai Institute of Applied Physics, Chinese Academy of Sciences, 201204 Shanghai, People's Republic of China*

Guang Xiong − *Department of Catalytic Chemistry and Engineering, State Key Laboratory of Fine Chemicals, Dalian University of Technology, 116024 Dalian, People's Republic of China*

Hong-bin Xie − *Key Laboratory of Industrial Ecology and Environmental Engineering, Department of Environmental Science and Technology, Dalian University of Technology, 116012 Dalian, People's Republic of China;* orcid.org/0000-0002-9119-9785

Complete contact information is available at:
https://pubs.acs.org/10.1021/acscatal.1c00126

Author Contributions

The manuscript was written through contributions of all authors. All authors have given approval to the final version of the manuscript.

Notes

The authors declare no competing financial interest.

REFERENCES

(1) International Energy Agency. Global CO_2 emissions in 2019; https://www.iea.org/articles/global-co2-emissions-in-2019 (accessed in October **2020**).

(2) Sanz-Pérez, E. S.; Murdock, C. R.; Didas, S. A.; Jones, C. W. Direct Capture of CO_2 From Ambient Air. *Chem. Rev.* **2016**, *116*, 11840−11876.

(3) Lee, S.-Y.; Park, S.-J. A Review on Solid Adsorbents for Carbon Dioxide Capture. *J. Ind. Eng. Chem.* **2015**, *23*, 1−11.

(4) Bui, M.; Adjiman, C. S.; Bardow, A.; Anthony, E. J.; Boston, A.; Brown, S.; Fennell, P. S.; Fuss, S.; Galindo, A.; Hackett, L. A.; Hallett, J. P.; Herzog, H. J.; Jackson, G.; Kemper, J.; Krevor, S.; Maitland, G.

C.; Matuszewski, M.; Metcalfe, I. S.; Petit, C.; Puxty, G.; Reimer, J.; Reiner, D. M.; Rubin, E. S.; Scott, S. A.; Shah, N.; Smit, B.; Martin Trusler, J. P.; Webley, P.; Wilcox, J.; Dowell, N. M. Carbon Capture and Storage (CCS): the Way Forward. *Energy Environ. Sci.* **2018**, *11*, 1062−1176.

(5) Vogt, C.; Groeneveld, E.; Kamsma, G.; Nachtegaal, M.; Lu, L.; Kiely, C. J.; Berben, P. H.; Meirer, F.; Weckhuysen, B. M. Unravelling Structure Sensitivity in CO₂ Hydrogenation Over Nickel. *Nat. Catal.* **2018**, *1*, 127−134.

(6) Kenarsari, S. D.; Yang, D.; Jiang, G.; Zhang, S.; Wang, J.; Russell, A. G.; Wei, Q.; Fan, M. Review of Recent Advances in Carbon Dioxide Separation and Capture. *RSC Adv.* **2013**, *3*, 22739−22773.

(7) Li, K.; Peng, B.; Peng, T. Recent Advances in Heterogeneous Photocatalytic CO₂ Conversion to Solar Fuels. *ACS Catal.* **2016**, *6*, 7485−7527.

(8) Gao, P.; Dang, S.; Li, S.; Bu, X.; Liu, Z.; Qiu, M.; Yang, C.; Wang, H.; Zhong, L.; Han, Y.; Liu, Q.; Wei, W.; Sun, Y. Direct Production of Lower Olefins from CO₂ Conversion *via* Bifunctional Catalysis. *ACS Catal.* **2018**, *8*, 571−578.

(9) Sen, R.; Goeppert, A.; Kar, S.; Surya Prakash, G. K. Hydroxide Based Integrated CO₂ Capture from Air and Conversion to Methanol. *J. Am. Chem. Soc.* **2020**, *142*, 4544−4549.

(10) Gao, P.; Li, S.; Bu, X.; Dang, S.; Liu, Z.; Wang, H.; Zhong, L.; Qiu, M.; Yang, C.; Cai, J.; Wei, W.; Sun, Y. Direct Conversion of CO₂ Into Liquid Fuels with High Selectivity over a Bifunctional Catalyst. *Nat. Chem.* **2017**, *9*, 1019−1024.

(11) Aresta, M.; Dibenedetto, A.; Angelini, A. Catalysis for the Valorization of Exhaust Carbon: from CO₂ to Chemicals, Materials, and Fuels. Technological Use of CO₂. *Chem. Rev.* **2014**, *114*, 1709−1742.

(12) Graciani, J.; Mudiyanselage, K.; Xu, F.; Baber, A. E.; Evans, J.; Senanayake, S. D.; Stacchiola, D. J.; Liu, P.; Hrbek, J.; Fernández Sanz, J.; Rodriguez, J. A. Highly Active Copper-Ceria and Copper-Ceria-Titania Catalysts for Methanol Synthesis from CO₂. *Science* **2014**, *345*, 546−550.

(13) Studt, F.; Sharafutdinov, I.; Abild-Pedersen, F.; Elkjær, C. F.; Hummelshøj, J. S.; Dahl, S.; Chorkendorff, I.; Nørskov, J. K. Discovery of a Ni-Ga Catalyst for Carbon Dioxide Reduction to Methanol. *Nat. Chem.* **2014**, *6*, 320−324.

(14) Martin, O.; Martín, A. J.; Mondelli, C.; Mitchell, S.; Segawa, T. F.; Hauert, R.; Drouilly, C.; Curulla-Ferré, D.; Pérez-Ramírez, J. Indium Oxide as a Superior Catalyst for Methanol Synthesis by CO₂ Hydrogenation. *Angew. Chem., Int. Ed.* **2016**, *55*, 6261−6265.

(15) Preti, D.; Resta, C.; Squarcialupi, S.; Fachinetti, G. Carbon Dioxide Hydrogenation to Formic Acid by Using a Heterogeneous Gold Catalyst. *Angew. Chem., Int. Ed.* **2011**, *50*, 12551−12554.

(16) Moret, S.; Dyson, P. J.; Laurenczy, G. Direct Synthesis of Formic Acid from Carbon Dioxide by Hydrogenation in Acidic Media. *Nat. Commun.* **2014**, *5*, 4017.

(17) Zhang, S.; Kang, P.; Meyer, T. J. Nanostructured Tin Catalysts for Selective Electrochemical Reduction of Carbon Dioxide to Formate. *J. Am. Chem. Soc.* **2014**, *136*, 1734−1737.

(18) Ansari, M. B.; Min, B.-H.; Mo, Y.-H.; Park, S.-E. CO₂ activation and promotional effect in the oxidation of cyclic olefins over mesoporous carbon nitrides. *Green Chem.* **2011**, *13*, 1416−1421.

(19) Ma, Z.; Porosoff, M. D. Development of tandem catalysts for CO₂ hydrogenation to olefins. *ACS Catal.* **2019**, *9*, 2639−2656.

(20) Satthawong, R.; Koizumi, N.; Song, C.; Prasassarakich, P. Light olefin synthesis from CO₂ hydrogenation over K-promoted Fe-Co bimetallic catalysts. *Catal. Today* **2015**, *251*, 34−40.

(21) Najjar, Y. S. H. Hydrogen Safety: The Roadmap Toward Green Technology. *Int. J. Hydrogen Energy* **2013**, *38*, 10716−10728.

(22) Rahmani, F.; Haghighi, M.; Mohammadkhani, B. Enhanced Dispersion of Cr Nanoparticles over Nanostructured ZrO₂-Doped ZSM-5 Used in CO₂-Oxydehydrogenation of Ethane. *Microporous Mesoporous Mater.* **2017**, *242*, 34−49.

(23) Porosoff, M. D.; Myint, M. N. Z.; Kattel, S.; Xie, Z.; Gomez, E.; Liu, P.; Chen, J. G. Identifying Different Types of Catalysts for CO₂ Reduction by Ethane through Dry Reforming and Oxidative Dehydrogenation. *Angew. Chem., Int. Ed.* **2015**, *54*, 15501−15505.

(24) Koirala, R.; Buechel, R.; Pratsinis, S. E.; Baiker, A. Silica is Preferred over Various Single and Mixed Oxides as Support for CO₂-Assisted Cobalt-Catalyzed Oxidative Dehydrogenation of Ethane. *Appl. Catal., A* **2016**, *527*, 96−108.

(25) Taghavinezhad, P.; Haghighi, M.; Alizadeh, R. Sonosynthesis of VOₓ/MCM-41 Nanocatalyst Enhanced by Various Metal Oxides (Mg, Al, Zr) for CO₂-Oxidative Dehydrogenation of Ethane to Ethylene. *Microporous Mesoporous Mater.* **2018**, *261*, 63−78.

(26) Cheng, Y.; Lei, T.; Miao, C.; Hua, W.; Yue, Y.; Gao, Z. Single-Site CrOₓ Moieties on Silicalite: Highly Active and Stable for Ethane Dehydrogenation with CO₂. *Catal. Lett.* **2018**, *148*, 1375−1382.

(27) Koirala, R.; Buechel, R.; Krumeich, F.; Pratsinis, S. E.; Baiker, A. Oxidative Dehydrogenation of Ethane with CO₂ over Flame-Made Ga-Loaded TiO₂. *ACS Catal.* **2015**, *5*, 690−702.

(28) Kim, S.; Mehran, M.; Mushtaq, U.; Lim, T.; Lee, J.; Lee, S.; Park, S.; Song, R. Effect of Reverse Boudouard Reaction Catalyst on the Performance of Solid Oxide Carbon Fuel Cells Integrated with a Dry Gasifier. *Energy Convers. Manage.* **2016**, *130*, 119−129.

(29) Rout, K.; Gil, M.; Chen, D. Highly Selective CO Removal by Sorption Enhanced Boudouard Reaction for Hydrogen Production. *Catal. Sci. Technol.* **2019**, *9*, 4100−4107.

(30) Baroi, C.; Gaffney, A. M.; Fushimi, R. Process Economics and Safety Considerations for the Oxidative Dehydrogenation of Ethane Using the M1 Catalyst. *Catal. Today* **2017**, *298*, 138−144.

(31) Mimura, N.; Okamoto, M.; Yamashita, H.; Oyama, S. T.; Murata, K. Oxidative Dehydrogenation of Ethane Over Cr/ZSM-5 Catalysts Using CO₂ as an Oxidant. *J. Phys. Chem. B* **2006**, *110*, 21764−21770.

(32) Park, M. S.; Chang, J.-S.; Kim, D. S.; Park, S.-E. Oxidative Dehydrogenation of Ethylbenzene with Carbon Dioxide over Zeolite-Supported Iron Oxide Catalysts. *Res. Chem. Intermed.* **2002**, *28*, 461−469.

(33) Zheng, H.; Lin, Y.; Wang, M.; Liu, J.; Wu, D.; Chen, J.; Yin, G.; Oyama, S. T.; Zhao, S. The Influence of Solvent Polarity on the Dehydrogenation of Isoborneol over a Cu/ZnO/Al₂O₃ Catalyst. *Catal. Today* **2019**, *323*, 44−53.

(34) Honda, Y.; Takagaki, A.; Kikuchi, R.; Oyama, S. T. Oxidative Dehydrogenation of Ethane Using Ball-Milled Hexagonal Boron Nitride. *Chem. Lett.* **2018**, *47*, 1090−1093.

(35) Dixit, M.; Kostetskyy, P.; Mpourmpakis, G. Structure-Activity Relationships in Alkane Dehydrogenation on γ-Al₂O₃: Site-Dependent Reactions. *ACS Catal.* **2018**, *8*, 11570−11578.

(36) Wu, J.; Peng, Z.; Bell, A. T. Effects of Composition and Metal Particle Size on Ethane Dehydrogenation over PtₓSn100-x/Mg (Al) O (70< x < 100). *J. Catal.* **2014**, *311*, 161−168.

(37) Yan, B.; Yao, S.; Kattel, S.; Wu, Q.; Xie, Z.; Gomez, E.; Liu, P.; Su, D.; Chen, J. G. Active Sites for Tandem Reactions of CO₂ Reduction and Ethane Dehydrogenation. *Proc. Natl. Acad. Sci. U. S. A.* **2018**, *115*, 8278−8783.

(38) Sun, P.; Siddiqi, G.; Vining, W. C.; Chi, M.; Bell, A. T. Novel Pt/Mg (In)(Al)O Catalysts for Ethane and Propane Dehydrogenation. *J. Catal.* **2011**, *282*, 165−174.

(39) Lisi, L.; Marchese, L.; Pastore, H. O.; Frache, A.; Ruoppolo, G.; Russo, G. Evaluating the Catalytic Performances of SAPO-34 Catalysts for the Oxidative Dehydrogenation of Ethane. *Top. Catal.* **2003**, *22*, 95−99.

(40) Yao, S.; Yan, B.; Jiang, Z.; Liu, Z.; Wu, Q.; Lee, J.; Chen, J. G. Combining CO₂ Reduction with Ethane Oxidative Dehydrogenation by Oxygen-Modification of Molybdenum Carbide. *ACS Catal.* **2018**, *8*, 5374−5381.

(41) Cheng, Y.; Miao, C.; Hua, W.; Yue, Y.; Gao, Z. Cr/ZSM-5 for Ethane Dehydrogenation: Enhanced Catalytic Activity Through Surface Silanol. *Appl. Catal., A* **2017**, *532*, 111−119.

(42) Zones, S. I. Zeolite SSZ-13 and its Method of Preparation. US Patent 4544538, 1985.

(43) Beale, A. M.; Gao, F.; Lezcano-Gonzalez, I.; Peden, C. H. F.; Szanyi, J. Recent Advances in Automotive Catalysis for NOₓ Emission

Control by Small-Pore Microporous Materials. *Chem. Soc. Rev.* **2015**, *44*, 7371−7405.

(44) Paolucci, C.; Khurana, I.; Parekh, A. A.; Li, S.; Shih, A. J.; Li, H.; Di Iorio, J. R.; Albarracin-Caballero, J. D.; Yezerets, A.; Miller, J. T.; Delgass, W. N.; Ribeiro, F. H.; Schneider, W. F.; Gounder, R. Consequences of Exchange-Site Heterogeneity and Dynamics on the UV-Visible Spectrum of Cu-Exchanged SSZ-13. *Chem. Sci.* **2017**, *357*, 898−903.

(45) Kim, Y. J.; Lee, J. K.; Min, K. M.; Hong, S. B.; Nam, I.-S.; Cho, B. K. Hydrothermal Stability of Cu-SSZ13 for Reducing NO_x by NH_3. *J. Catal.* **2014**, *311*, 447−457.

(46) Hudson, M. R.; Queen, W. L.; Mason, J. A.; Fickel, D. W.; Lobo, R. F.; Brown, C. M. Unconventional, Highly-Selective CO_2 Adsorption in Zeolite SSZ-13. *J. Am. Chem. Soc.* **2012**, *134*, 1970−1973.

(47) Liu, J.; He, N.; Zhou, W.; Lin, L.; Liu, G.; Liu, C.; Wang, J.; Xin, Q.; Xiong, G.; Guo, H. Isobutane Aromatization Over a Complete Lewis Acid Zn/HZSM-5 Zeolite Catalyst: Performance and Mechanism. *Catal. Sci. Technol.* **2018**, *8*, 4018−4029.

(48) Liu, J.; He, N.; Zhou, W.; Shu, M.; Lin, L.; Wang, J.; Si, R.; Xiong, G.; Xin, Q.; Guo, H. Operando Dual Beam FTIR Spectroscopy Unravels the Promotional Effect of Zn on HZSM-5 in Isobutane Aromatization. *Catal. Sci. Technol.* **2019**, *9*, 1609−1620.

(49) Almutairi, S. M. T.; Mezari, B.; Magusin, P. C. M. M.; Pidko, E. A.; Hensen, E. J. M. Structure and Reactivity of Zn-Modified ZSM-5 Zeolites: The Importance of Clustered Cationic Zn Complexes. *ACS Catal.* **2012**, *2*, 71−83.

(50) Brunauer, S.; Emmett, P. H.; Teller, E. Adsorption of Gases in Multimolecular Layers. *J. Am. Chem. Soc.* **1938**, *60*, 309−319.

(51) Lippens, B. C.; Deboer, J. H. Studies on Pore Systems in Catalysts: The V-t Method. *J. Catal.* **1965**, *4*, 319−323.

(52) Frisch, M. J.; Trucks, G. W.; Schlegel, H. B.; Scuseria, G. E.; Robb, M. A.; Cheeseman, J. R.; Scalmani, G.; Barone, V.; Mennucci, B.; Petersson, G. A.; Nakatsuji, H., et al. *Gaussian 09, Rev. A.1*; Gaussian, Inc.: Wallingford, CT, 2009.

(53) Ananikov, V. P.; Musaev, D. G.; Morokuma, K. Real Size of Ligands, Reactants and Catalysts: Studies of Structure, Reactivity and Selectivity by ONIOM and Other Hybrid Computational Approaches. *J. Mol. Catal. A: Chem.* **2010**, *324*, 104−119.

(54) Chai, J.-D.; Head-Gordon, M. Long-Range Corrected Hybrid Density Functionals with Damped Atom-Atom Dispersion Corrections. *Phys. Chem. Chem. Phys.* **2008**, *10*, 6615−6620.

(55) Pidko, E. A.; van Santen, R. A. Activation of Light Alkanes Over Zinc Species Stabilized in ZSM-5 Zeolite: a Comprehensive DFT Study. *J. Phys. Chem. C* **2007**, *111*, 2643−2655.

(56) Bader, R. F. W.; Carroll, M. T.; Cheeseman, J. R.; Chang, C. Properties of Atoms in Molecules: Atomic Volumes. *J. Am. Chem. Soc.* **1987**, *109*, 7968−7979.

(57) Vilé, G.; Albani, D.; Nachtegaal, M.; Chen, Z.; Dontsova, D.; Antonietti, M.; López, N.; Pérez-Ramírez, J. A Stable Single-Site Palladium Catalyst for Hydrogenations. *Angew. Chem., Int. Ed.* **2015**, *54*, 11265−11269.

(58) Giannakakis, G.; Flytzani-Stephanopoulos, M.; Sykes, E. C. H. Single-Atom Alloys as a Reductionist Approach to the Rational Design of Heterogeneous Catalysts. *Acc. Chem. Res.* **2019**, *52*, 237−247.

(59) Bligaard, T.; Bullock, R. M.; Campbell, C. T.; Chen, J. G.; Gates, B. C.; Gorte, R. J.; Jones, C. W.; Jones, W. D.; Kitchin, J. R.; Scott, S. L. Toward Benchmarking in Catalysis Science: Best Practices, Challenges, and Opportunities. *ACS Catal.* **2016**, *6*, 2590−2602.

(60) Liu, J.; He, N.; Zhou, W.; Lin, L.; Liu, G.; Liu, C.; Wang, J.; Xin, Q.; Xiong, G.; Guo, H. Isobutane Aromatization Over a Complete Lewis Acid Zn/HZSM-5 Zeolite Catalyst: Performance and Mechanism. *Catal. Sci. Technol.* **2018**, *8*, 4018−4029.

(61) Liu, J.; He, N.; Zhao, Y.; Lin, L.; Zhou, W.; Xiong, G.; Xie, H.; Guo, H. The Crucial Role of Skeleton Structure and Carbon Number on Short-Chain Alkane Activation over Zn/HZSM-5 Catalyst: An Experimental and Computational Study. *Catal. Lett.* **2018**, *148*, 2069−2081.